

Predicting Frictional Properties of Graphene Kirigami Using Molecular Dynamics and Neural Networks

Designs for a negative friction coefficient.

Mikkel Metzsch Jensen



Thesis submitted for the degree of
Master in Computational Science: Materials Science
60 credits

Department of Physics
Faculty of mathematics and natural sciences

UNIVERSITY OF OSLO

Spring 2023

Predicting Frictional Properties of Graphene Kirigami Using Molecular Dynamics and Neural Networks

Designs for a negative friction coefficient.

Mikkel Metzsch Jensen



© 2023 Mikkel Metzsch Jensen

Predicting Frictional Properties of Graphene Kirigami Using Molecular Dynamics and Neural Networks

<http://www.duo.uio.no/>

Printed: Reprocentralen, University of Oslo

Abstract

Abstract.

Acknowledgments

Acknowledgments.

List of Symbols

F_N Normal force (normal load)

Acronyms

CNN Convolutional Neural Network. 12

MD Molecular Dynamics. 5, 12, 19, 25

ML Machine Learning. 21, 22, 23, 24, 25

MSE Mean Squared Error. 14

Contents

I	Background Theory	1
II	Simulations	3
1	Kirigami configuration exploration	5
1.1	Generating the dataset	5
1.2	Data analysis	6
1.3	Properties of interest	8
1.4	Machine learning	12
1.4.1	Architecture	12
1.4.2	Data handling	13
1.4.2.1	Input	13
1.4.2.2	Output	13
1.4.2.3	Data augmentation	13
1.4.3	Loss	14
1.4.4	Hypertuning	14
1.4.5	Final model	20
1.5	Accelerated Search	24
1.5.1	Patteren generation search	24
1.5.2	Genetic algorithm search	27
A	Appendices	31
A	Appendix A	33
A	Appendix B	35
B	Appendix C	37

Part I

Background Theory

Part II

Simulations

Chapter 1

Kirigami configuration exploration

Building upon the discoveries of the Pilot Study ??, we will further explore the impact of Kirigami designs on strain-dependent friction. Our focus is primarily to optimize the friction force and friction coefficient towards their maximum or minimum values. To achieve this goal, we will utilize MD simulations to generate an extended dataset that encompasses a wider range of Kirigami designs. This is motivated by the aim of gaining gain a broader understanding of the friction-strain relationship. We will then leverage this dataset to explore the potential of employing machine learning for predicting friction behavior based on Kirigami design, strain, and load. Finally, we plan to utilize the developed machine learning model for an accelerated search.

1.1 Generating the dataset

We aim to create a dataset that contains an extended series of Kirigami design configurations based on the pattern generation methods developed in ?? for which we will vary the strain and load for each configuration. For each configuration, we sample 15 pseudo uniform strain values (see ??) between zero and the rupture strain according to the rupture test. Since the normal force did not prove to be dominant in the friction description we only sample 3 values per configuration, uniformly sampled in the range [0.1, 10] nN. In total, this gives $3 \times 15 = 45$ data points for each configuration. For the remaining parameters, we use the values presented in the pilot study (see ??). We are mainly concerned with the mean friction and whether the sheet ruptures during the simulation. However, we also include the maximum friction, the relative contact, the rupture strain (from the rupture test) and the porosity (void fraction) in the dataset. We generate 68 configurations of the Tetrahedron pattern type, 45 of the Honeycomb type and 100 of the Random walk type. For the Tetrahedron and Honeycomb patterns, we choose a random reference position that results in translation of the patterns. A summary of the dataset is given in Table 1.1 while all configurations are shown visually in ???. The Tetrahedron and Honeycomb parameters are chosen to provide additional variations of the configurations evaluated in ?? which exhibited interesting properties. The Random walk configurations are chosen with the aim of introducing as much variety as possible within our Random walk framework. Notice that not all submitted data points “make it” to the final dataset. This is due to a small bug in the data generation procedure¹.

¹The issue arises from the fact that the rupture point in the rupture test does not completely match the rupture point in the following simulations. After performing the rupture test the simulation is restarted with a new substrate size, corresponding to the measured rupture strain limit, but also with a new random velocity and thermostat initialization. The sheet is then strained and checkpoints of the simulation state (LAMMPS restart files) are stored for each of the targeted strain samples. However, if the rupture point arrives earlier than suggested by the rupture test, due to randomness from the initialization, some of the planned strain samples do not get a corresponding checkpoint file. Thus, these data points are not included in the dataset even though they ideally should have been noted as a rupture event. This could quite have been mitigated by a rewrite of the code, but it was first discovered after the dataset had been created. We notice, however, that the dataset still contains 11.57 % rupture events which provide a reasonable amount of rupture events to incorporate in the machine learning model

Table 1.1: Summary of the number of generated data points in the dataset. Due to slight deviations in the rupture strain and the specific numerical procedure not all submitted simulations “make it” to the final dataset. Notice that the Tetrahedon (7, 5, 2) and Honeycomb (2, 2, 1, 5) from the pilot study are rerun as a part of the Tetrahedon and the Honeycomb datasets separately. In the latter datasets, the reference point for the pattern is randomized and thus these configurations are not fully identical. This is the reason for the ambiguousness in the total sum.

Type	Configurations	Submitted data points	Final data points	Ruptures
Pilot study	3	270	261	25 (9.58 %)
Tetrahedon	68	3060	3015	391 (12.97 %)
Honeycomb	45	2025	1983	80 (4.03 %)
Random walk	100	4500	4401	622 (14.13 %)
Total	214 (216)	9855	9660	1118 (11.57 %)

1.2 Data analysis

In order to gain insight into the correlations in the data we calculate the correlation coefficients between all variable combinations. More specifically, we calculate the Pearson product-moment correlation coefficient which is defined, between data set X and Y , as

$$\text{corr}(X, Y) = \frac{\text{Cov}(X, Y)}{\sigma_X \sigma_Y} = \frac{\langle (X - \mu_X)(Y - \mu_Y) \rangle}{\sigma_X \sigma_Y} \in [-1, 1],$$

where $\text{Cov}(X, Y)$ is the covariance, μ the mean value and σ the standard deviation. The correlation coefficients range from a perfect negative correlation (-1) through no correlation (0) to a perfect positive correlation (1). The correlation coefficients are shown in Fig. 1.1.

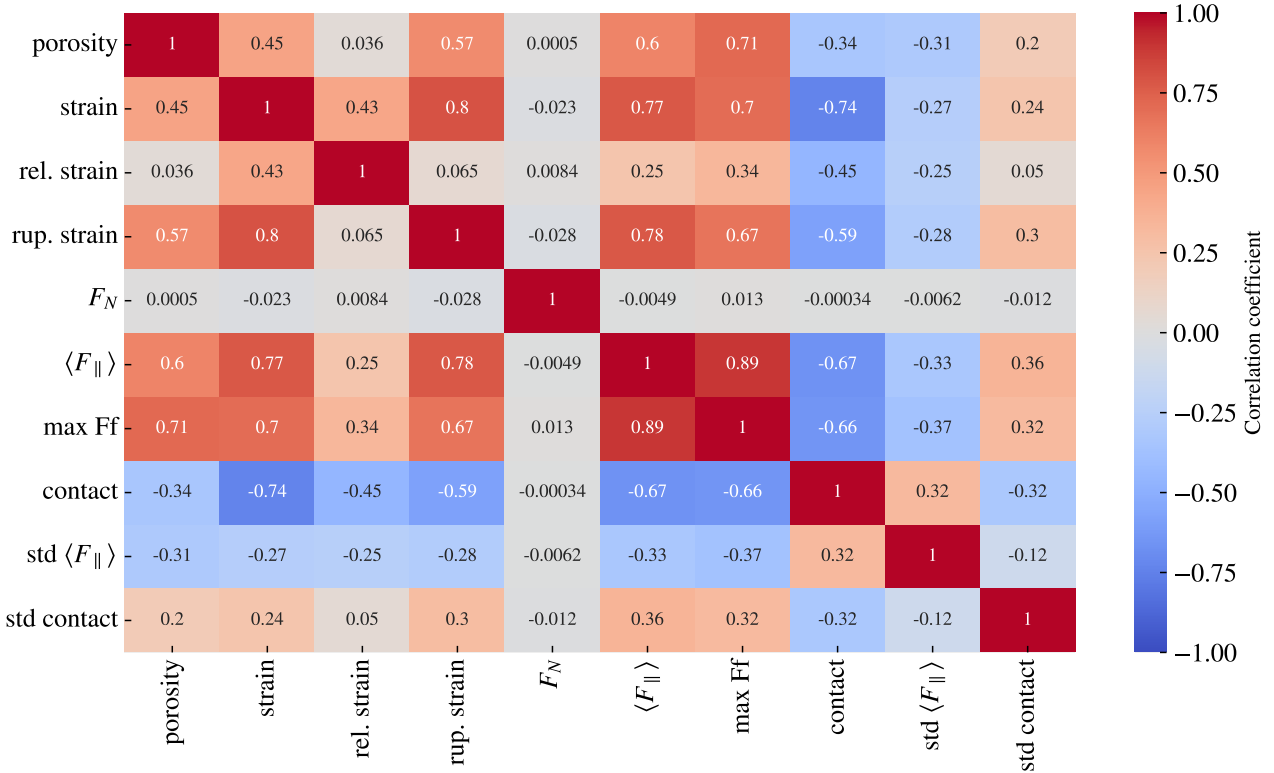


Figure 1.1: Pearson product-moment correlation coefficients for the full dataset (see Table 1.1).

From Fig. 1.1 we especially notice that the mean friction force $\langle F_{\parallel} \rangle$ has a significant positive correlation with strain (0.77) and porosity (0.60). However, the relative strain, the strain scaled by the rupture strain, has a weaker correlation of only 0.25. This indicates that the correlation might be associated with the flexibility of the configurations since these can be taken to higher absolute values of strain. This is further supported by the fact that the mean friction and the rupture strain are also strongly positively correlated (0.78). From Fig. 1.1 we also observe that the contact is negatively correlated with the mean friction (-0.67) and the strain value (-0.74). This is generally consistent with the trend observed in the pilot study in ?? where the increasing strain was correlated with a decreasing contact and mainly increasing mean friction. However, we must note that the correlation coefficient is a measure of the strength and slope of a forced linear fit on the data. Since we have observed a non-linear trend between friction and strain (??) we should not expect any near 100 % correlations. Additionally, we also notice that all correlations to normal load are rather low, which aligns well with the findings in the pilot study.

Fig. 1.2 shows a visualization of the data (excluding the pilot study configurations) for chosen variable pairs on the axes. This provides a visual clue on some of the correlations and provides a qualitative feeling for the diversity in various planes of the feature space that we eventually will base our machine learning model on. We notice that the honeycomb pattern is spanning a significantly larger range of strain, contact and mean friction.

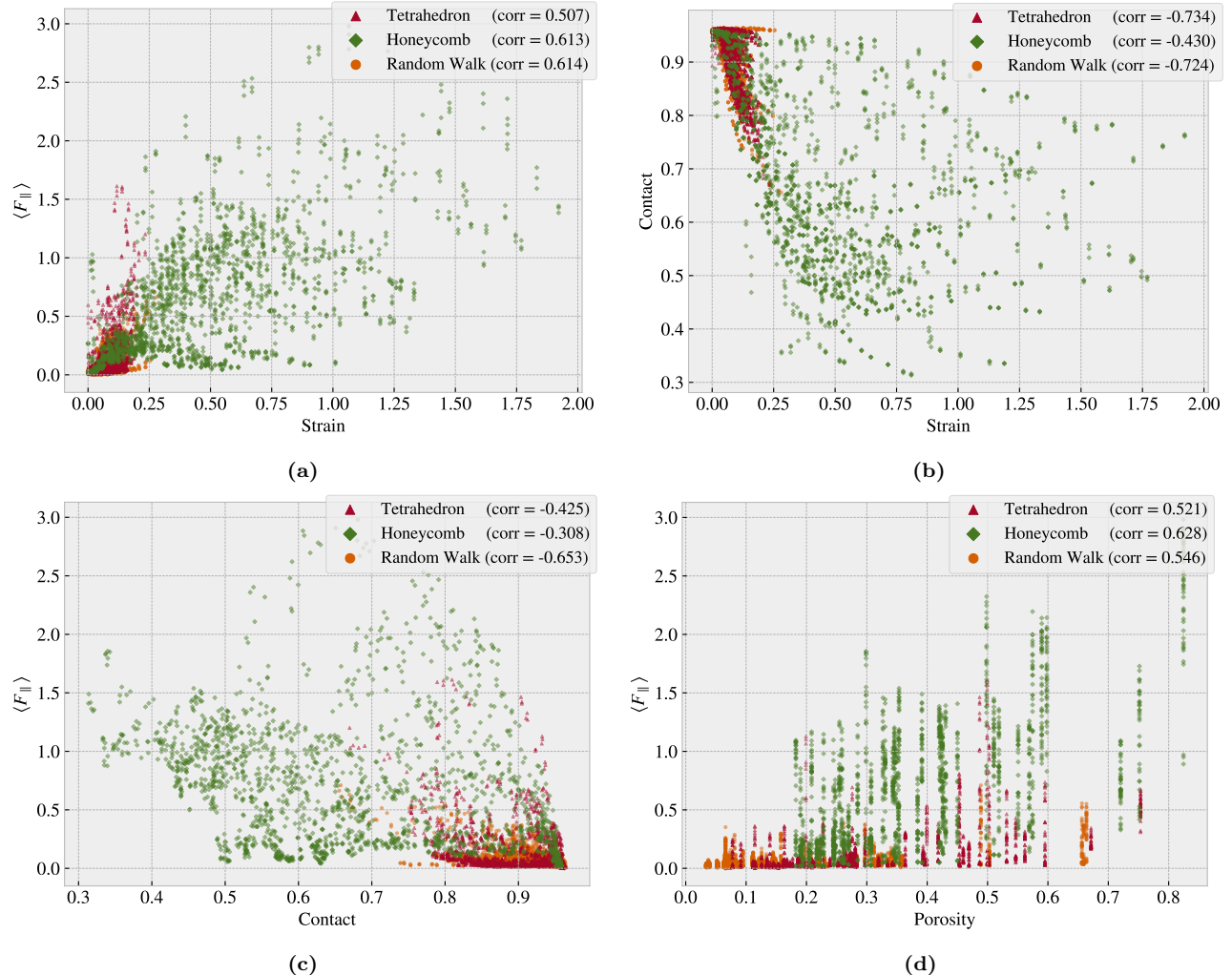


Figure 1.2: Scatter plot of the data sets Tetrahedron, Honeycomb and Random Walk (excluding the pilot study) for various variable combinations in order to visualize some chosen correlations of interest and distributions in the data

1.3 Properties of interest

In the pilot study (??) we found promising results for the idea of achieving a negative friction coefficient under the assumption of a system with coupled normal force and strain. Hence, we will consider this as a main property of interest for our further exploration. However, it is not obvious how one should rigorously quantify this. The friction coefficient is by our definition (??) given as the slope of the friction F_f vs. normal force F_N curve. Hence, for two data points $\{(F_{N,1}, F_{f,1}), (F_{N,2}, F_{f,2})\}$, $F_{N,1} < F_{N,2}$ we can evaluate the associated friction coefficient $\mu_{1,2}$ as

$$\mu_{1,2} = \frac{F_{f,2} - F_{f,1}}{F_{N,2} - F_{N,1}} = \frac{\Delta F_f}{\Delta F_N}.$$

In the pilot study, it became apparent that the effects of friction under the change of load is negligible in comparison to the effects related to strain ε . Thus, by working under the assumption $F(F_N, \varepsilon) \sim F(\varepsilon)$ and a coupling $F_N \propto R \cdot \varepsilon$ with linear coupling ratio R we get

$$\mu_{1,2}(\varepsilon_1, \varepsilon_2) = \frac{\Delta F_f(\varepsilon_1, \varepsilon_2)}{R(\varepsilon_2 - \varepsilon_1)} \propto \frac{\Delta F_f(\varepsilon_1, \varepsilon_2)}{\Delta \varepsilon}. \quad (1.1)$$

With this reasoning, we can in practice substitute load F_N for strain ε in the expression for the friction coefficient of our coupled system. This justifies the search for a negative slope on the friction-strain curve since this can be related to a negative friction coefficient in our proposed coupled system. The remaining question is then how to evaluate the strength of this property. By definition, the minimum (most negative) slope value would give the lowest friction coefficient. However, two data points with a small $\Delta\varepsilon$, corresponding to a small denominator in Eq. (1.1), would potentially lead to a huge negative slope value without any significant decrease in friction. Hence, we choose to consider the drop in friction with increasing strain as a better metric. Numerically we compute this by locating the local maxima on the friction-strain curve and then evaluating the difference to the succeeding local minima. The biggest difference corresponds to the *max drop* which serves as our indicator for a negative friction coefficient. In this evaluation, we do not guarantee a monotonic decrease of friction in the range of the biggest drop, but when searching among multiple configurations this is considered a decent strategy to highlight configurations of interest worthy of further investigation. In addition to the biggest drop in friction, we also consider the minimum, $\min F_{\text{fric}}$, and maximum, $\max F_{\text{fric}}$, friction along with the maximum difference, $\max \Delta f_{\text{fric}} = \max F_{\text{fric}} - \min F_{\text{fric}}$. The extrema of these four properties for each of the categories: Tetrahedron, Honeycomb, Random walk and Pilot study, are summarized in Table 1.2. The corresponding strain profiles and configurations are shown in Fig. 1.3 to 1.6 (excluding the pilot study). The strain profiles for the full dataset are shown in appendix ??.

From the property comparison in Table 1.2 we find that both the Tetrahedron and Honeycomb subsets contain improved candidates for each of the property scores in comparison to the Tetrahedron (7, 5, 1) and Honeycomb (2, 2, 1, 5) examined in the pilot study. Overall, the Honeycomb pattern type is still resulting in the highest scores for the maximum properties while the minimum friction is still achieved by the non-cut sheet. This latter observation reveals that our dataset does not provide any indication that friction can readily be reduced for a Kirigami sheet under strain. However, the improvement in the remaining properties indicates that the dataset contains the necessary information to provide a direction for further optimization of the maximum properties. Considering the Random walk we find that the max property scores are generally lower than that of the Tetrahedron and Honeycomb structures. However, since these are found to be on a comparable order of magnitude we argue that contain relevant information for populating configuration space with respect to machine learning training. The Random walk patterns also contribute with some immediate insight into the structures that we can associate with each of the properties of interest due to its increased diversity in comparison to the other patterns.

For the $\min F_{\text{fric}}$ top candidates (Fig. 1.3) we find that the Random walk candidate has a rather cut density (low porosity) and with vertical cuts. Since these cuts run parallel to the stretching direction one can hypothesize that this minimizes the induced buckling effect which agrees with the constant level of contact. For the minimum candidate for the Tetrahedron pattern, we also observe a low decrease in contact, and in both these cases this corresponds with a relatively flat friction-strain curve. When considering the remaining friction-strain curve throughout Fig. 1.3 to 1.6 we find a rising friction-strain curve which is accompanied by a decreasing relative contact. When looking at the Random walk 96 pattern, which is the top candidate for both the $\max F_{\text{fric}}$ (Fig. 1.4) and $\max \Delta f_{\text{fric}}$ (Fig. 1.5) property, we find a rather porous configuration with mainly horizontal-orientated cuts.

This has some structural reminiscence with the Honeycomb pattern. Finally, the best random walk candidate for the max drop category, Random walk 01, did not produce a big drop. We find that the contact area is decreasing with strain but not as strongly as seen for the other configurations. The configuration contains some slanted cuts which might be reminiscent of parts of the Tetrahedron pattern.

Table 1.2: Evaluation of the properties of interest for our dataset.

Tetrahedron	Configuration	Strain	Value [nN]	Hon. (2, 2, 1, 5) [nN]
$\min F_{\text{fric}}$	(3, 9, 4)	0.0296	0.0067	0.0262
$\max F_{\text{fric}}$	(5, 3, 1)	0.1391	1.5875	0.8891
$\max \Delta F_{\text{fric}}$	(5, 3, 1)	[0.0239, 0.1391]	1.5529	0.8603
max drop	(5, 3, 1)	[0.1391, 0.1999]	0.8841	0.5098

Honeycomb	Configuration	Strain	Value [nN]	Tetra. (7, 5, 1) [nN]
$\min F_{\text{fric}}$	(2, 5, 1, 1)	0.0267	0.0177	0.0623
$\max F_{\text{fric}}$	(2, 1, 1, 1)	1.0654	2.8903	1.5948
$\max \Delta F_{\text{fric}}$	(2, 1, 5, 3)	[0.0856, 1.4760]	2.0234	1.5325
max drop	(2, 3, 3, 3)	[0.5410, 1.0100]	1.2785	0.9674

Random walk	Configuration	Strain	Value [nN]
$\min F_{\text{fric}}$	12	0.0562	0.0024
$\max F_{\text{fric}}$	96	0.2375	0.5758
$\max \Delta F_{\text{fric}}$	96	[0.0364, 0.2375]	0.5448
max drop	01	[0.0592, 0.1127]	0.1818

Pilot study	Configuration	Strain	Value [nN]
$\min F_{\text{fric}}$	No cut	0.2552	0.0012
$\max F_{\text{fric}}$	Honeycomb	0.7279	1.5948
$\max \Delta F_{\text{fric}}$	Honeycomb	0.7279	1.5325
max drop	Honeycomb	[0.7279, 1.0463]	0.9674

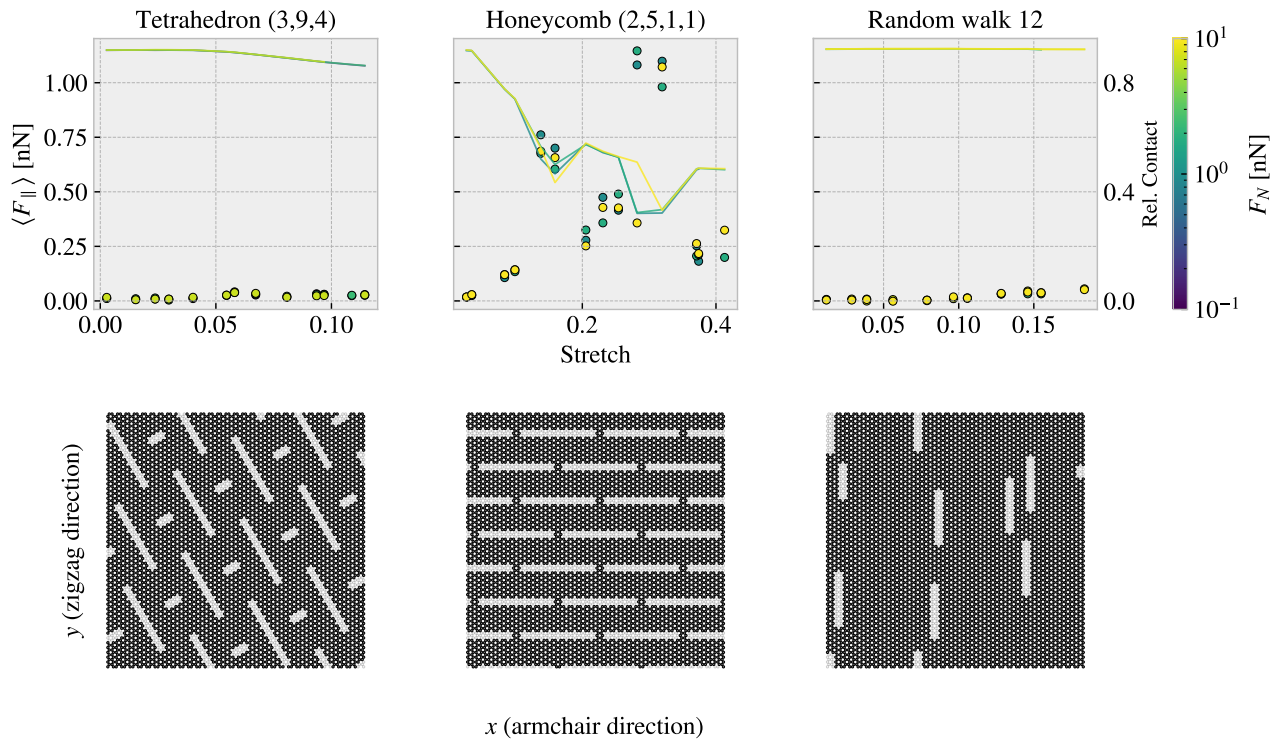


Figure 1.3: Minimum friction: Configurations corresponding to the minimum friction.

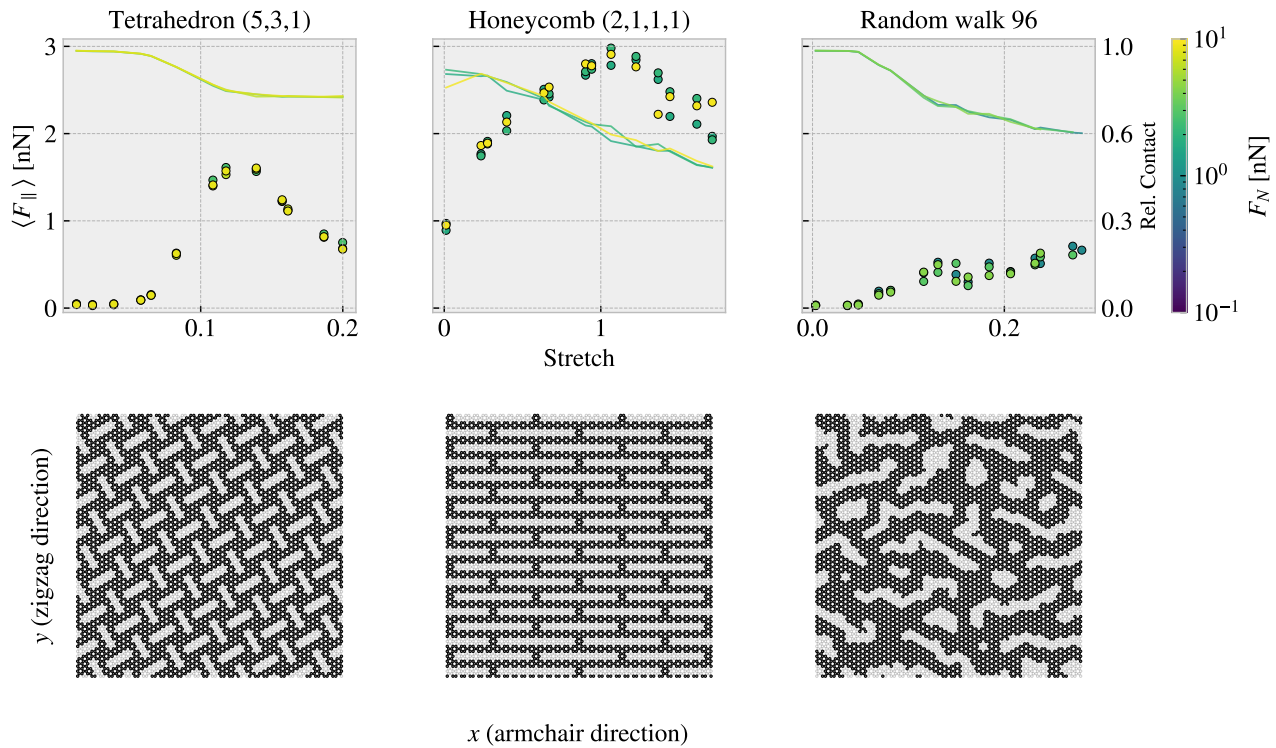


Figure 1.4: Maximum friction: Configurations corresponding to the maximum friction.

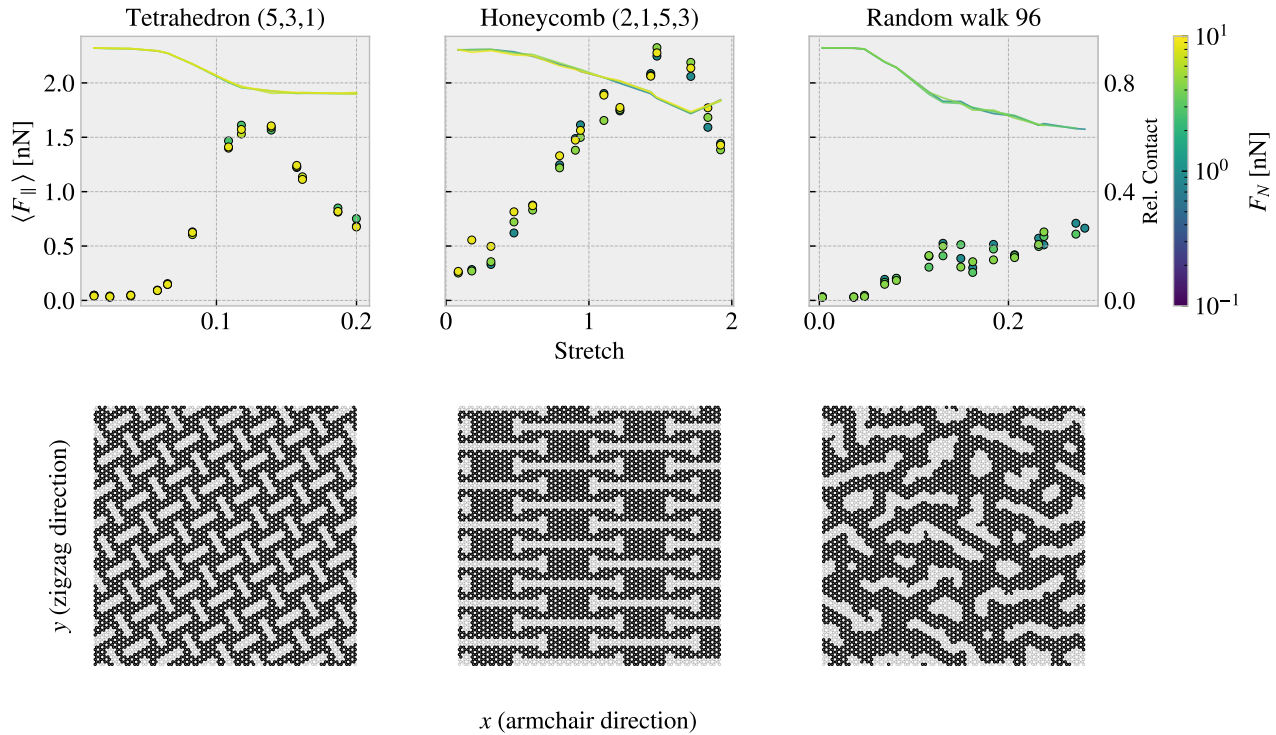


Figure 1.5: Maximum Difference: Configurations corresponding to the biggest difference in friction in the dataset for each pattern.

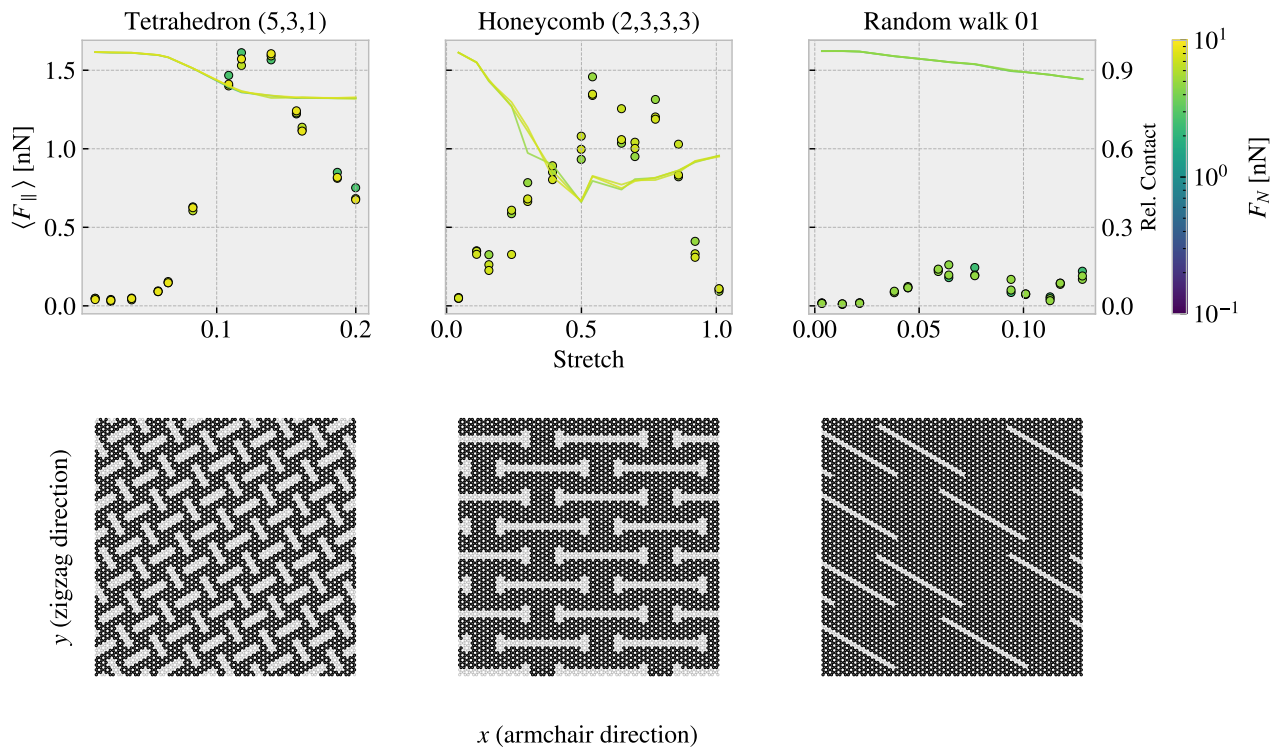


Figure 1.6: Maximum drop: Configurations corresponding to the biggest friction drop in the dataset for each pattern.

1.4 Machine learning

Given the MD-based dataset we investigate the possibilities of training a machine learning model to predict the friction behaviour from a given Kirigami configuration, strain and load.

1.4.1 Architecture

Due to the spatial dependencies in the Kirigami configurations, we use a convolutional neural network (CNN) for our model architecture. Similar studies which predict mechanical properties for graphene sheets have used a VGGNet style network, Hanakata et al. [1, 2] and Wan et al. [3], which we adopt for this study as well. The VGGNet-16 architecture illustrated in Fig. 1.7 shows the key features that we will include:

- The image is processed through a series of 3×3 convolutional filters (the smallest size capable of capturing spatial dependencies) using a stride of 1 with an increasing number of channels throughout the network. Each convolutional layer is followed by a ReLU activation function.
- The spatial dimensions are reduced by a max pooling, filter size 2×2 and a stride of 2, which halves the spatial resolution each time.
- The latter part of the network consists of a fully connected part followed by a ReLU activation. The transition from the convolutional to the fully connected part is achieved by applying a filter with the same dimensions as the last convolutional feature map. This essentially maps the spatial output to the fully connected layer with the number of channels corresponding to the nodes in this layer.

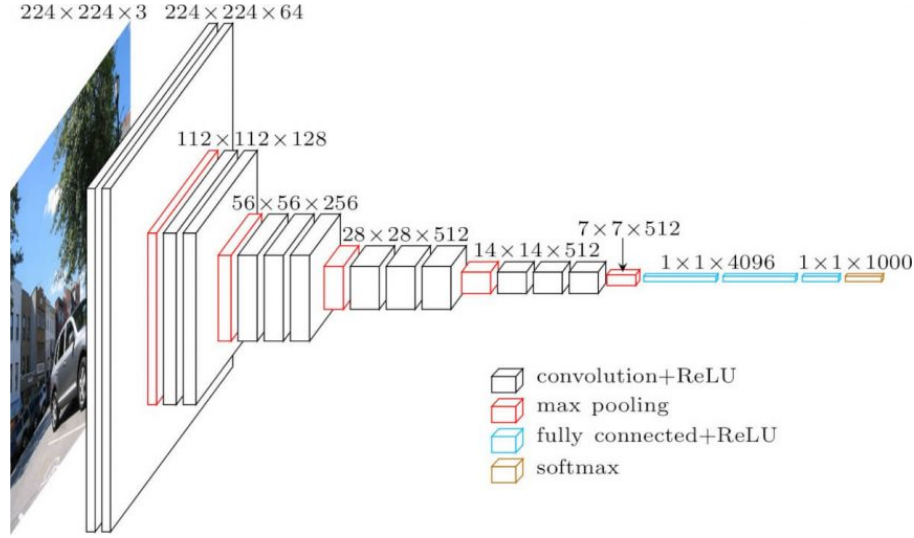


Figure 1.7: VGGNet 16. Source <https://neurohive.io/en/popular-networks/vgg16/>.

We deviate from the VGGNet-16 architecture by including batch normalization and restricting ourselves to build the convolutional part in terms of the blocks: (Convolution \rightarrow Batch normalization \rightarrow ReLU \rightarrow Max pooling). Similarly, we define a fully connected block by two elements (Fully connected \rightarrow ReLU) which match the VGGNet model. Hanakata et al. and Wan et al. used a similar architecture with the parameters

$$\begin{array}{ll} \text{Hanakata et al. [1]} & C16\ C32\ C64\ D64, \\ \text{Wan et al. [3]} & C16\ C32\ D32\ D16, \end{array}$$

Where C denotes a convolutional block with the number denoting the number of channels, and D a fully connected (dense) block with the number denoting number of nodes. For the process of determining a suiting complexity for the architecture, we adopt the approach by Wan et al. [3] who used a “staircase” pattern for combining convolutional and fully connected blocks. By defining a starting number of channels S and network depth D we fill the first half with convolutional blocks doubling in channel number for each layer and the latter

half with fully connected blocks having the number of nodes decreasing in a reverse pattern. For instance the architecture $S4D8$ will take the form Following this pattern a ($S = 4, D = 8$) would take the form

$$\text{Input} \rightarrow \underbrace{\overset{S=4}{C4 \ C8 \ C16 \ C32}}_{D=8} \underbrace{\overset{D=8}{D32 \ D16 \ D8 \ D4}} \rightarrow \text{Output.}$$

This provides a simple description where S and D can be varied systematically for a grid search over architecture complexity.

1.4.2 Data handling

1.4.2.1 Input

We use three variables as input: Kirigami configuration, strain of the sheet and applied normal load. While the first is a two-dimensional input the latter are both scalars. This gives rise to two main options for the data structure

1. Expand the scalar values (strain and load) into 2D matrices of the same size as the Kirigami configuration (copying the scalar value to all positions). This can then be merged into an image of three channels used as a single input.
2. Pass only the Kirigami configuration through the convolutional part of the network and introduce the remaining scalar values into the fully connected part of the network halfway in.

Both options utilize the same data, but the first is more appropriate if the configuration should be considered in context with the applied strain and load, while the latter corresponds to a more independent processing. We implemented both options but it was immediately clear from the test runs that option 1 was producing the most promising result which we settled on.

1.4.2.2 Output

For the output we are mainly concerned with mean friction and the rupture detection. In combination, this will make the model able to produce a friction vs. strain curve with an estimated stopping point as well. However, for some cases, the model can benefit from having additional output variables to adjust for **source**, and thus we include we include maximum friction, contact, porosity and rupture strain in the output as well. This also gives us more options for exploring the relationship in the data later on. Notice that we weight the importance of these output variables different in the loss as described in variables differently as described in Sec. 1.4.3.

Removed this part, do you think it has any relevance: Notice that the rupture strain refers to the value found in the rupture test without load, but as the sheet always ruptures before or just around this point in a loaded state this provides some information for the training to lean on, even though it is in the output state. In principle, we could add a penalty whenever the network predicts the sheet to be attached for strain values above the rupture strain, but we found the performance of the rupture prediction to be satisfactory without such penalties.

1.4.2.3 Data augmentation

In order to increase the utility of the available data one can introduce data augmentation. For most classification tasks this usually includes distortions such as color shifts, zoom, flip etc. However, such distortions are only valid since the classification network should still classify a cat as a cat even though it is suddenly a bit brighter or flipped upside down. For our problem, we can only use augmentation that matches a physical symmetry. Such a symmetry exists for reflection across the y-axis. We cannot do this across the x-axis as the sheet is translated in a positive y-direction meaning that the reflected version would correspond to a change in the sliding direction which we cannot expect to be fully symmetric.

1.4.3 Loss

The output contains two different types of variables: scalar values and binary values (0: False 1: True). For the scalar values we use the Mean Squared Error (MSE)

$$L_{\text{MSE}} = \frac{1}{N} \sum_{i=1}^N (y_i - \hat{y}_i)^2,$$

where N is the number of data entries, y are the true output and \hat{y} are the predicted values. For the binary output, we use binary cross entropy

$$L_{\text{BCE}} = -\frac{1}{N} \left[\sum_{i=1}^N [t_i \log(p_i) + (1 - t_i) \log(1 - p_i)] \right],$$

where $t \in \{0, 1\}$ is the truth label. Does this belong in theory entirely? I do introduce it there but I guess I have to mention the choice here still. We calculate the total loss as a weighted sum of the loss associated with each variable

$$L_{\text{tot}} = \sum_v W_v \cdot L_v.$$

We choose the weights to be 1/2 for the mean friction and 1/10 for the remaining 5 variables, thus sharing the loss evenly for the remaining 50% of the weight. During the introductory phase of the training, we tried different settings for these weights. We found that the results varied little and concluded that the training is not very sensitive to this choice, for which we stuck with the values defined above.

1.4.4 Hypertuning

For the hypertuning we focus on architecture complexity, learning rate, momentum and weight decay. Thus the non-changing elements are the use of the ADAM optimizer with the initial default values of $\beta_1 = 0.9$, $\beta_2 = 0.999$ and zero weight decay (we will change momentum β_1 and weight decay). We use a batch size of 32 and train the model for a maximum of 1000 epochs, but we save the best model during training based on the lowest validation loss.

Since the learning rate is considered to be one of the most important hyperparameters we will determine a suitable choice for the learning rate using the learning rate range test for each of the two major grid searches:

1. Architecture complexity grid search of S vs. D with individually chosen learning rates for each complexity combination.
2. Momentum vs. weight decay grid search with learning range chosen with regard to the momentum.

We consider first the architectures in the range $S \times D = \{2, 4, 8, 16, 32, 64, 128, 256\} \times \{4, 6, 8, 10, 12, 14\}$. For each architecture complexity, we perform an initial learning rate range test, increasing the learning rate until the training loss diverges. The suggested learning rate is then determined as the point for which the training loss decreases most rapidly. The learning rate is increased exponentially within the range 10^{-7} to 10 with increments for each training batch iteration. This is done for just a single epoch where a training batch size of 32 yields a total of 242 increments. This corresponds to an exponent increment of approximately 1/30 giving a relative increase $10^{1/30} \sim 108\%$ per batch iteration. The learning rate range test is presented in Fig. 1.8 for various model architectures. We notice that the suggested learning rate decreases with an increasing number of model parameters. This decrease is further independent of the specific relationship between S and D .

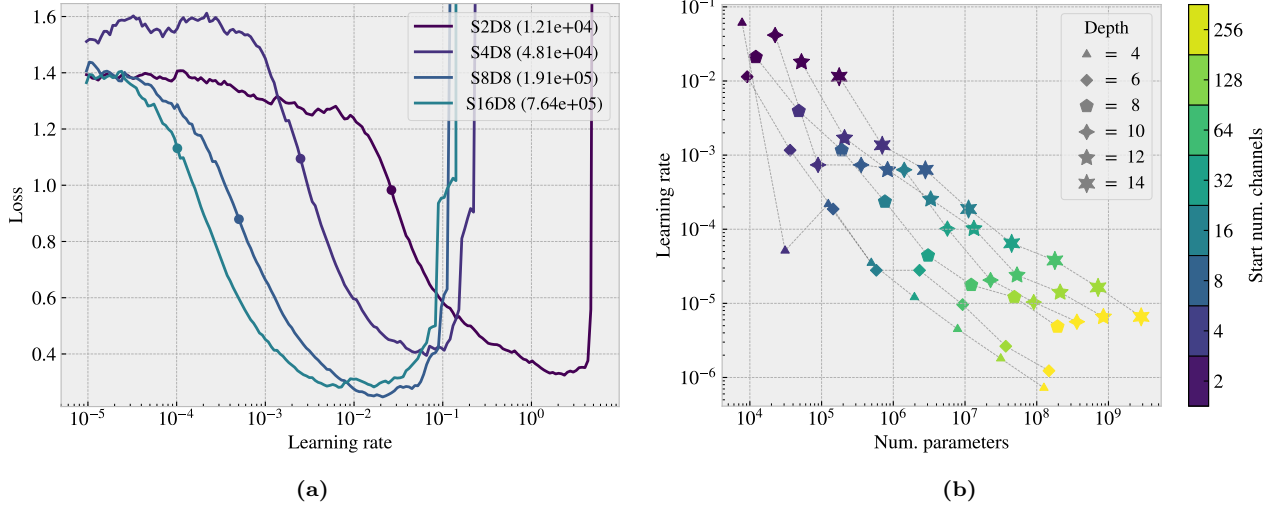


Figure 1.8: Learning rate range test for various model complexities. We increase the learning rate exponentially from nume-7 to 10 during one epoch corresponding to an exponent increment of roughly 1/30 per batch iteration. (a) shows a few examples of the training loss history as a function of learning rate. The examplatory architectures are S[2, 16]D8 with the corresponding number of model parameters shown in parentheses in the legend. The dot indicates the suggested learning rate at the steepest decline of the slope. (b) shows the full results of suggested learning rates depending on the number of model parameters with color coding differentiating the number of start channels and marker types differentiating different model depths.

With the use of the suggested learning rates from Fig. 1.8 we perform a grid search over the corresponding S and D parameters. We evaluate both the loss and the mean friction R_2 score for the validation data which is shown in Fig. 1.9 together with the best epoch and the number of model parameters. Additionally, we evaluate the mean friction R_2 score for a selected set of configurations. This set consists of the top 10 configurations with respect to maximum friction drop for the Tetrahedron and Honeycomb pattern respectively. This is done as a way of evaluating the performance on the non-linear strain curves which we immediately found to be the more difficult patterns to capture. The selected evaluation is shown in Fig. 1.10. Note that these patterns are already a part of the full dataset and thus the data points related to these patterns are most likely present in both the training and the validation data set. Hence, the performance must be considered in conjunction with the actual validation performance in Fig. 1.9.

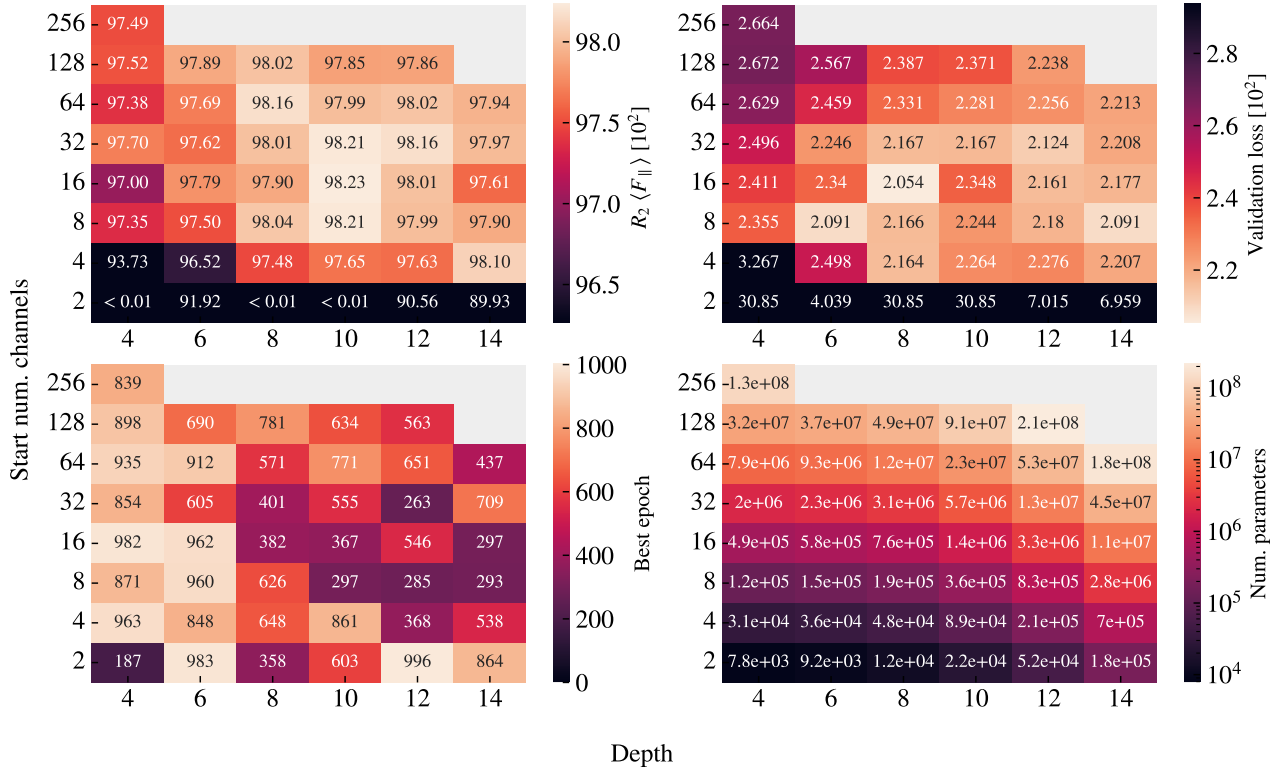
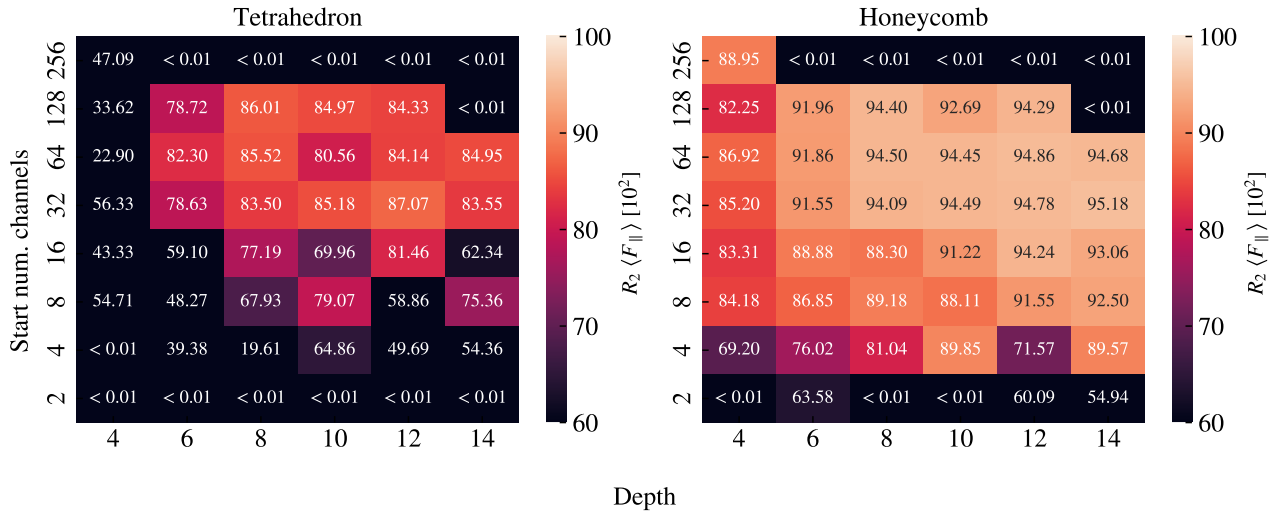


Figure 1.9: Architecture search.

Figure 1.10: Selected pseudo validation set. Fix the missing grey fields in the top which are replaced by $\downarrow 0.01$.

From the validation scores in Fig. 1.9 we find that models S(8-32)D(8-12) to give the best performance. When looking at the best epoch we find that models of low depth result in a later best epoch which is compatible with underfitting. As the depth is increased we find more models with a lower best epoch, in the range $\sim [300, 600]$, which on the other hand suggest cases of overfitting. Since our training stores the best model during training, we do not have to worry too much about overfitting, but we can take this transition from underfitting to overfitting as a sign that our search is conducted in an appropriate complexity range. When consulting the evaluation on the selected set in Fig. 1.10 we notice in general that we get significantly lower R_2 scores, especially for the

Tetrahedron pattern. Considering, that some of these data points are also present in the training data, this is a clear indication that these configurations are more challenging to predict. While the peak R_2 value for the validation score was found for the S16D10 model we see a slight preference for more complexity in the model with regard to the selected test. In the Tetrahedron selected set grid search, we find the best model to be S32D12, with a R_2 score of $\sim 87\%$. This model choice is more or less compatible with the overall performance as this is among the top candidates for the R_2 score and loss in Fig. 1.9 and the R_2 score for the Honeycomb pattern in Fig. 1.10 as well. Hence, we settle on this architecture.

Next, we consider momentum m and weight decays wd in the range $m \in [0.85, 0.99]$ and $wd \in [0, 1e-2]$. An increased momentum is expected to decrease the appropriate learning rate (check with theory), and thus we perform a new learning rate range test for each momentum choice. We propose two learning rate schemes: A constant learning rate as used until this point and a one-cycle policy. In the one-cycle policy we set a maximum bound for the learning rate and start from a factor 1/20 of this bound and increase towards the maximum bound during the first 30% of the training. For the final 70% of training we decrease towards a final minimum given as a factor $1e-4$ of the maximum bound. The increase and decrease are done by a cosine function. The suggested learning rate for the constant learning rate scheme is once again determined by the steepest slope on the loss curve while the maximum bound used for the one-cycle policy is determined as the point just before divergence. We find that the minimum point on the loss curve is a suitable choice that approaches the diverging point without getting too close and causing instabilities. The learning rate range test for momentum is shown in Fig. 1.11. We observe that a higher momentum gives higher suggested learning rates, so I need to check with theory on that. Using the results for the momentum learning rate range test we perform a grid search of momentum and weight decay. We examine again the validation loss and validation mean friction R_2 score in addition to the friction mean R_2 score for the selected set of Tetrahedron and Honeycomb patterns. This is shown for the constant learning rate scheme in Fig. 1.12 and for the cyclic scheme in Fig. 1.13.

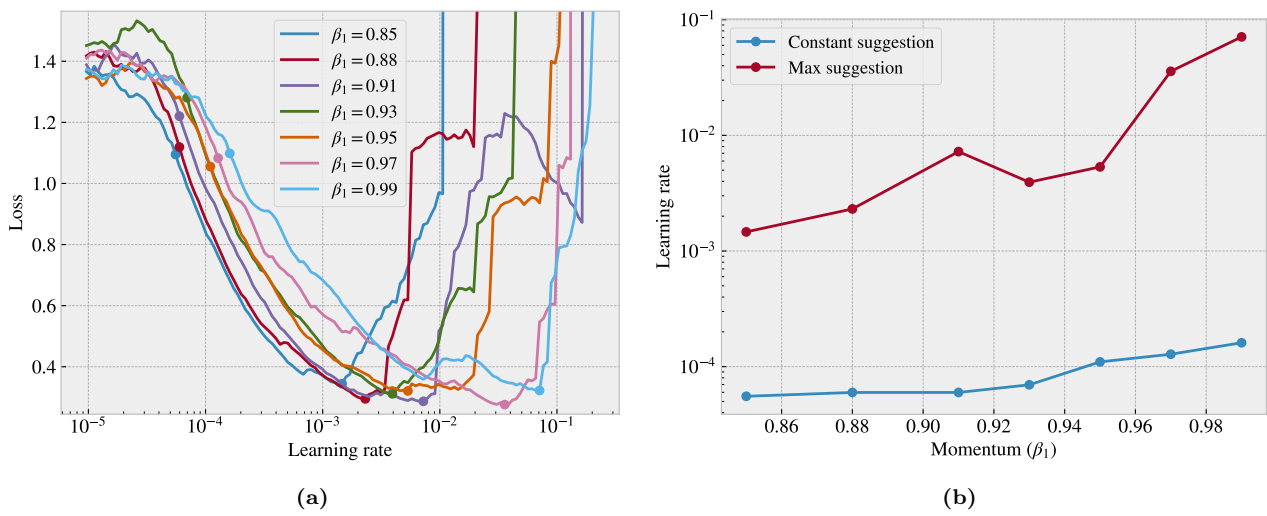


Figure 1.11: Momentum learning rate range tests

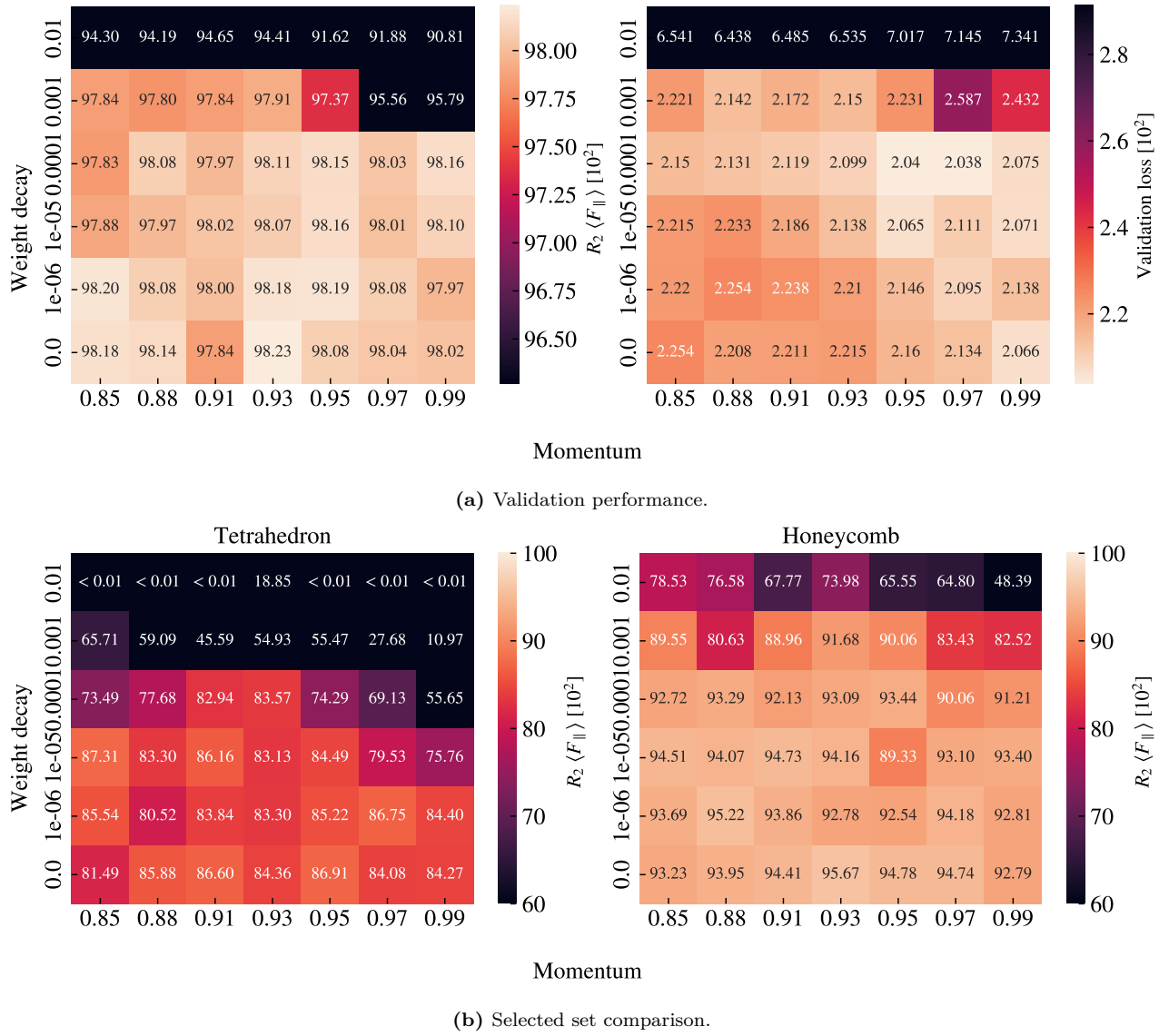


Figure 1.12: Constant learning rate and momentum scheme

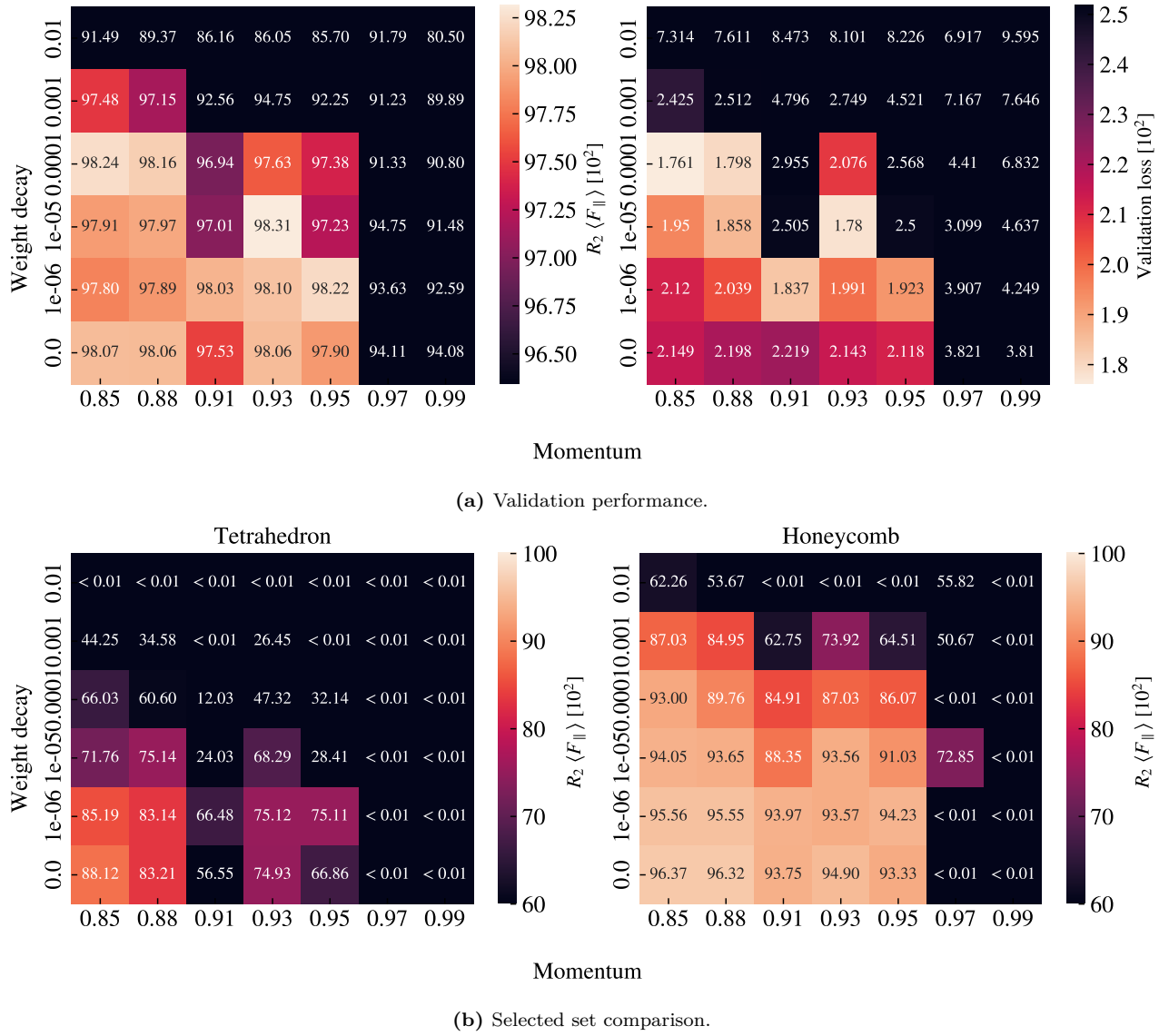


Figure 1.13: Cyclic learning rate and momentum scheme

The original validation scores, before varying momentum and weight decay, were a validation loss of 0.02124 and a mean friction R_2 score of 0.9816. By varying momentum and weight decay, we can improve these scores slightly for the constant learning rate scheme (loss: 0.02038, R_2 : 0.9823) and even more for the cyclic scheme (loss: 0.0176, R_2 : 0.9831). However, notice that these scores are taking for separate combinations of hyperparameters. The comparison among best scores is summarized in Table 1.3. In general, the constant scheme shows rather stable results for all momentum settings $m \in [0.85, 0.99]$ in combination with a low weight decay $wd \leq 10^{-4}$. For the cyclic scheme the performance peaks towards a low momentum $m \leq 0.93$ and low weight decay $wd \leq 10^{-4}$. Looking at the summary in Table 1.3 we see that the cyclic scheme can produce a high score among all four performance metrics, but since these scores do not share common hyperparameters we need to choose which of them to prioritize. Due to our interest in capturing the non-linear trends, we prioritize the score from the selected set of Tetrahedron patterns as this provided the greatest challenge for our model to capture. We recognize that this choice introduces a greater risk of overfitting since the data points are partly included in the training set. However, for the purpose of performing an accelerated search, we find it more important to increase the chances of discovering novel designs than to reduce the chance of getting false positive results. Since we have the option to verify the properties of a given design through MD simulations we do not have to rely on the machine learning prediction as a final score but only as a proposal for configurations worth further studying. Thus we choose the

cyclic trained model with low momentum $m = 0.85$ and zero weight decay as our final model. Finally, we note that since our choice of hyperparameters corresponded to the edge of our grid search it would have been natural to perform an extended search in that range. This was omitted due to time prioritization and the belief that the potential gain of doing so was not huge.

Table 1.3: Momentum and weight decay grid search using S32D12 model.

		Score [10 ²]	Momentum	Weight decay
Validation loss	Original	2.124	0.9	0
	Constant	2.038	0.97	10 ⁻⁴
	Cyclic	1.761	0.85	10 ⁻⁴
Validation R_2	Original	98.16	0.9	0
	Constant	98.23	0.93	0
	Cyclic	98.31	0.93	10 ⁻⁵
Tetrahedron R_2	Original	87.07	0.9	0
	Constant	87.31	0.85	10 ⁻⁵
	Cyclic	88.12	0.85	0
Honeycomb R_2	Original	94.78	0.9	0
	Constant	95.67	0.93	0
	Cyclic	96.37	0.85	0

1.4.5 Final model

From the hypertuning study, we choose the S32D12 model trained by a cyclic training scheme with a momentum of 0.85 and zero weight decay. The main performance metrics are shown in Table 1.4. Since the porosity is a number between 0 and 1 we can interpret the absolute error as the percentage error similar to the relative error for the rupture strain. The rupture strain is generally within a 13 % margin, but we believe that this number is especially high due to some low strain rupture cases in the dataset which contributes to a large relative error. The strain curves for mean friction, max friction and contact is shown in Fig. 1.14 in comparison with the Tetrahedron (7, 5, 1) and Honeycomb (2,2,1,5) used in the pilot study. This gives a visual interpretation of how well the fits are for the given R_2 , and we get a visual confirmation that a R_2 score above 0.98 indeed looks like a promising capture for the non-linear trends in the data. We will perform a true test set evaluation later on, based on some of the suggestions from the accelerated search.

Table 1.4: Mean values are used over different configurations.

	Loss [10 ²]	R_2 [10 ²]			Abs. [10 ²]	Rel. [10 ²]	Acc. [10 ²]
	Total	Mean F_f	Max F_f	Contact	Porosity	Rup. Strain	Rupture
Validation	2.1488	98.067	93.558	94.598	02.325	12.958	96.102
Tetrahedron	4.0328	88.662	85.836	64.683	01.207	05.880	99.762
Honeycomb	8.6867	96.627	89.696	97.171	01.040	01.483	99.111

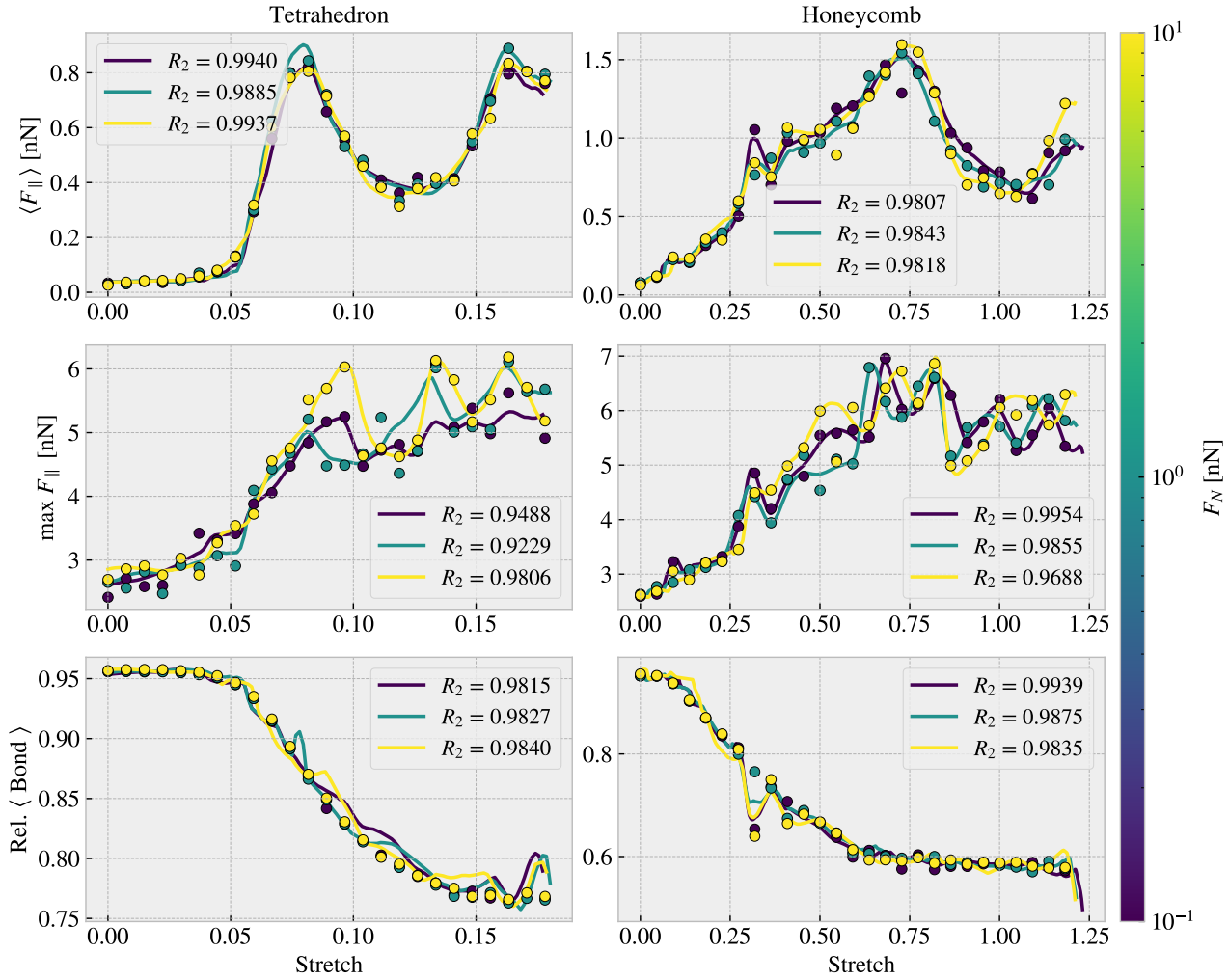


Figure 1.14: With 10^3 points in the strain range $[0, 1.5]$ and stopping after first rupture True prediction.

Using our final model, we evaluate the performance for the top ranking within the properties of interest. That is, we go through all the configurations in the dataset for the Tetrahedron (Table 1.5), Honeycomb (Table 1.6) and Random Walk (Table 1.7) patterns separately and rank the configurations in each property category. This is then compared to the actual ranking in the dataset. Generally, we find that the ML performs rather well in the ranking of the max, max difference and max drop properties, but it is deviating a bit more for the minimum friction property. This can be attributed to the fact that the precision needed for an accurate ranking among the minimum friction cases is a lot greater than for the remaining properties. The ML model gives mostly similar predictions for the max-categories ranking for the Tetrahedron and Honeycomb pattern but struggles a bit more for the Random Walk. Looking at the values for the top candidates in the max-types properties we see that it is generally within a ~ 0.2 nN range which is promising.

Table 1.5: Tetrahedon

ML Rank	Data		ML		Data Rank
	Config	Value [nN]	Config	Value [nN]	
min F_{fric}					
20	(3, 9, 4)	0.0067	(3, 1, 2)	0.0041	5
5	(3, 1, 3)	0.0075	(1, 3, 4)	0.0049	11
6	(5, 3, 4)	0.0084	(1, 3, 3)	0.0066	6
21	(1, 7, 3)	0.0084	(3, 1, 4)	0.0066	8
1	(3, 1, 2)	0.0097	(3, 1, 3)	0.0078	2
max F_{fric}					
1	(5, 3, 1)	1.5875	(5, 3, 1)	1.5920	1
2	(1, 3, 1)	1.4310	(1, 3, 1)	1.2739	2
4	(3, 1, 2)	1.0988	(9, 3, 1)	1.1162	4
3	(9, 3, 1)	1.0936	(3, 1, 2)	0.7819	3
5	(7, 5, 1)	0.7916	(7, 5, 1)	0.7740	5
max ΔF_{fric}					
1	(5, 3, 1)	1.5529	(5, 3, 1)	1.5578	1
2	(1, 3, 1)	1.3916	(1, 3, 1)	1.2331	2
4	(3, 1, 2)	1.0891	(9, 3, 1)	1.0807	4
3	(9, 3, 1)	1.0606	(3, 1, 2)	0.7778	3
5	(7, 5, 1)	0.7536	(7, 5, 1)	0.7399	5
max drop					
1	(5, 3, 1)	0.8841	(5, 3, 1)	0.8603	1
2	(3, 5, 1)	0.4091	(3, 5, 1)	0.3722	2
4	(7, 5, 1)	0.3775	(1, 1, 1)	0.2879	5
5	(9, 7, 1)	0.2238	(7, 5, 1)	0.2478	3
3	(1, 1, 1)	0.1347	(9, 7, 1)	0.1302	4

Table 1.6: Honeycomb

ML Rank	Data		ML		Data Rank
	Config	Value [nN]	Config	Value [nN]	
$\min F_{\text{fric}}$					
1	(2, 5, 1, 1)	0.0177	(2, 5, 1, 1)	0.0113	1
9	(2, 4, 5, 1)	0.0187	(2, 5, 5, 3)	0.0149	7
7	(2, 4, 1, 1)	0.0212	(2, 5, 5, 1)	0.0182	4
3	(2, 5, 5, 1)	0.0212	(2, 5, 3, 1)	0.0186	5
4	(2, 5, 3, 1)	0.0226	(2, 4, 1, 3)	0.0198	15
$\max F_{\text{fric}}$					
1	(2, 1, 1, 1)	2.8903	(2, 1, 1, 1)	2.9171	1
2	(2, 1, 5, 3)	2.2824	(2, 1, 5, 3)	2.4004	2
6	(2, 1, 3, 1)	2.0818	(2, 1, 5, 1)	2.1060	5
4	(2, 1, 3, 3)	2.0313	(2, 1, 3, 3)	1.9458	4
3	(2, 1, 5, 1)	2.0164	(2, 4, 1, 1)	1.9381	6
$\max \Delta F_{\text{fric}}$					
1	(2, 1, 5, 3)	2.0234	(2, 1, 5, 3)	2.1675	1
2	(2, 1, 1, 1)	1.9528	(2, 1, 1, 1)	2.0809	2
3	(2, 4, 1, 1)	1.8184	(2, 4, 1, 1)	1.9157	3
4	(2, 1, 3, 3)	1.7645	(2, 1, 3, 3)	1.6968	4
5	(2, 4, 1, 3)	1.4614	(2, 4, 1, 3)	1.5612	5
$\max \text{drop}$					
1	(2, 3, 3, 3)	1.2785	(2, 3, 3, 3)	1.3642	1
2	(2, 1, 3, 1)	1.1046	(2, 1, 3, 1)	0.9837	2
3	(2, 3, 3, 5)	0.8947	(2, 3, 3, 5)	0.9803	3
4	(2, 1, 5, 3)	0.8638	(2, 1, 5, 3)	0.9556	4
13	(2, 5, 1, 1)	0.8468	(2, 4, 5, 3)	0.8999	8

Table 1.7: RW

ML Rank	Data		ML		Data Rank
	Config	Value [nN]	Config	Value [nN]	
min F_{fric}					
1	12	0.0024	12	-0.0011	1
24	76	0.0040	06	0.0036	27
6	13	0.0055	14	0.0074	23
31	08	0.0065	05	0.0082	19
26	07	0.0069	63	0.0085	57
max F_{fric}					
3	96	0.5758	99	0.5155	2
1	99	0.5316	98	0.4708	3
2	98	0.4478	96	0.4356	1
4	97	0.3624	97	0.3503	4
11	58	0.3410	55	0.2817	7
max ΔF_{fric}					
3	96	0.5448	99	0.4669	2
1	99	0.4769	98	0.4314	3
2	98	0.4085	96	0.4128	1
4	97	0.3268	97	0.3080	4
78	57	0.2978	55	0.2542	7
max drop					
3	01	0.1818	00	0.1883	3
2	96	0.1733	96	0.1654	2
1	00	0.1590	01	0.1532	1
11	37	0.1022	04	0.0591	8
28	34	0.0879	56	0.0552	20

1.5 Accelerated Search

Having trained a machine learning (ML) model we use it for an extended accelerated search for further optimization of the friction properties of interest. We approach this search by two different methods:

1. Using the generative algorithms developed for the creation of the Tetrahedron, Honeycomb and Random walk patterns, we create yet an extended dataset and evaluate the performance using the ML.
2. Using the genetic algorithm method we perpetuate the configurations and optimize for the maximum drop property using the ML model to evaluate the fitness function.

1.5.1 Patteren generation search

We utilize the pattern generators to create an extended dataset for our search. For the Tetrahedron and Honeycomb patterns, the increment of the parameters will eventually lead to the main structures becoming so large they do exceed the size of the sheet. Thus, we can essentially perform a full search “maxing out” the parameters of these patterns. We estimate that this is done with the max parameters, (60, 60, 30) for the Tetrahedron, and ([30, 30, 30, 60]) for the Honeycomb. We use a random reference position and regenerate each unique parameter 10 times to explore translational effects. This gives in total 135k configurations for the Tetrahedron pattern and 2025k for the Honeycomb pattern. For the Random walk generator, we do a Monte Carlo sampling. In each sample, we draw the scalar values, either from a uniform (U) or logarithmic uniform (LU) distribution as follows.

$$\text{Num. walks} \sim U[1, 30]$$

$$\text{Max. steps} \sim U[1, 30]$$

$$\text{Min. dis.} \sim U[0, 4]$$

$$\text{Bias direction} \sim U[0, 2\pi]$$

$$\text{Bias. strength} \sim LU[0, 10]$$

$$p_{\text{stay}} \sim U[0, 1]$$

Notice that we use discrete distribution for the parameters requiring integers. For the binary parameters *Connection*, *Avoid invalid*, *RN6* and *Grid start* we simply set the values by a 50–50 chance. The remaining parameters are kept constant at *Periodic: True* and *Centering:False* throughout the search. For the handling of clustering, we implement the repair algorithm such that the sheet is repaired by the least modifications approach rather than retrying the generation several times **Make sure that this is introduced somewhere**. Due to the extra computation time associated with the random walk and the repair algorithm, we only generate 10k configurations within this class. For the evaluation of the configurations we use a normal load of 5 nN and generate a strain curve in the domain 0–200 % using 100 evenly spaced points. Top candidate results for each property are shown in Table 1.8 including a comparison to the dataset top candidates originally shown in Table 1.2. The random walk top five candidates are visualized in Fig. 1.16.

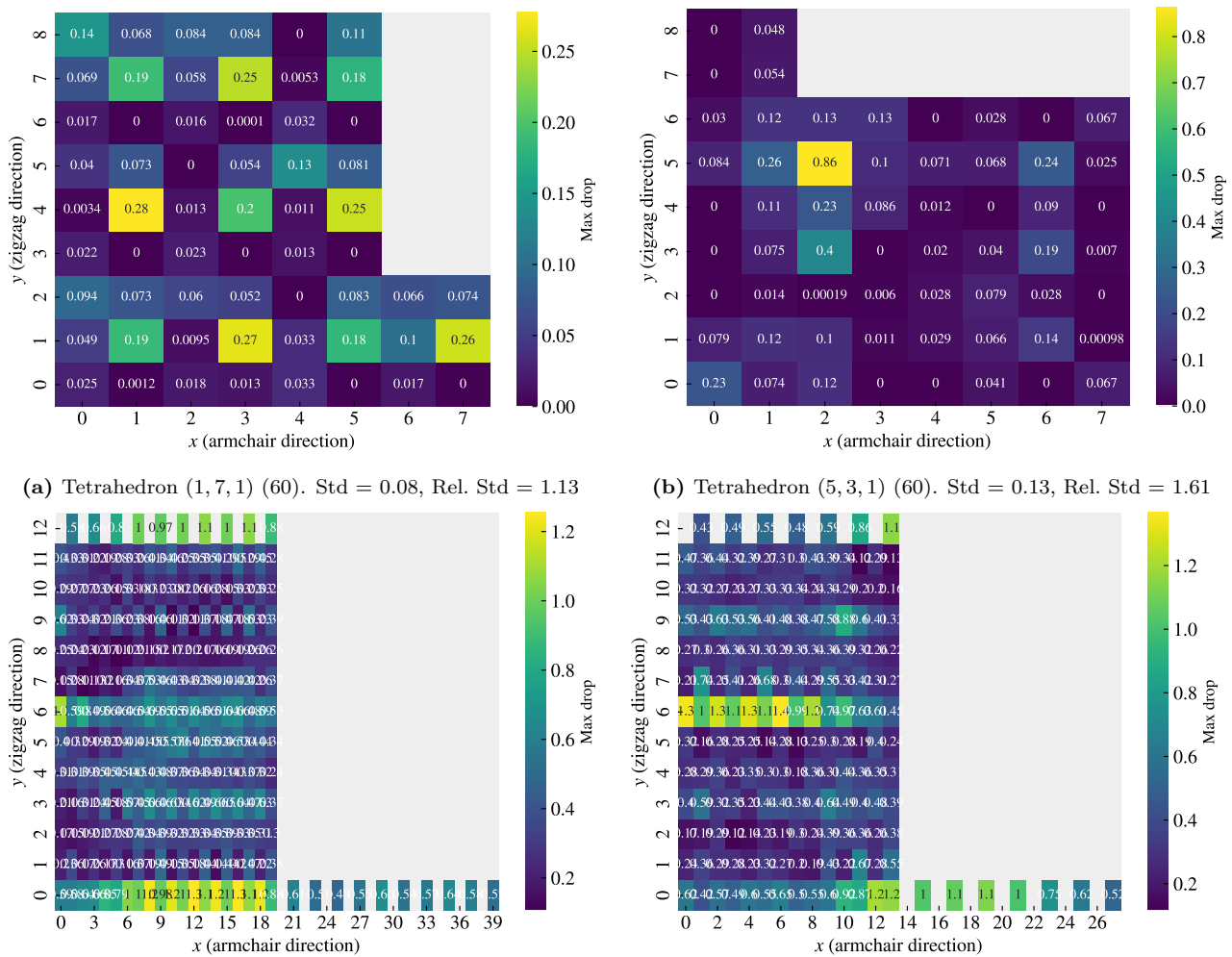
First of all, the search shows a rather consistent result regarding the minimization of friction where the top candidates all share the same feature of being sparsely cut. For the Random walk, we see this visually in Fig. 1.16, while for the Tetrahedron and Honeycomb patterns, this is evident from the configuration parameters shown in Table 1.8 where the parameters reveal a high spacing between the cuts. The porosity of the minimum friction top candidates are all rather low being 1.5%, 5.6%, and 1.6% for the Tetrahedron, Honeycomb and Random walk respectively. These results point toward Kirigami modifications not being applicable for a lowering of friction, within the limitations of our numerical setup. This is in agreement with the initial analysis on the MD dataset, and hence the dataset does not provide evident suggestions for friction minimization. Thus we might argue that the model is limited on the dataset for this property. The fact that the top candidates all take negative values also shows that the model is not reliable in this domain. By asking for the lowest friction we effectively take advantage of the sparsely populated areas of the model parameter space which can lead to unphysical predictions. In order to resolve this problem one might attempt an extension of the dataset and possibly also applying a physical constraint for positive friction values.

Among the remaining maximum-type properties, we find competing values for the Honeycomb and Random walk classes. When taking a closer look at the ranking for each property it becomes apparent that the predictions are highly sensitive to the reference position parameters used for the Tetrahedron and Honeycomb pattern. Since we repeated each pattern parameter 10 times for random reference positions, we initially expected to get a ranking in sets of 10. However, the ranking shows contiguous appearing sets in the range 1–5 which points toward a sensitivity for pattern translation. Hence we investigate this further by evaluating the scores for a systematic change of the reference position for selected configurations. We generally fix the max drop parameter to give the highest variation and thus we show scores for the max drop top candidates, Tetrahedron (1, 7, 1), (5, 3, 1) and Honeycomb (3, 3, 5, 3), (2, 3, 3, 3), in Fig. 1.15. It becomes evident that the predictions vary drastically with the translation of these patterns. The emerging question is then whether this is actually grounded in a physical phenomenon or simply a deficiency in the ML. Even though the patterns are periodic in the x-y-plane, with period matching the unique translations shown in Fig. 1.15, the translation will determine the specific configuration of the edge. Previous studies of static friction and stick-slip behavior point to the importance of edge effects **look back at theory and maybe source**, and thus for a sheet where the atoms sitting on the $\pm x$ free sides constitutes about 2.5% of the inner sheet atom count, it is not unreasonable that the translation might result in a significantly different outcome. In that case, the search through reference positions highlights that the translation can be key to optimizing for certain properties. However, the results might also indicate that the model is either overfitted or that we simply did not provide enough data to reach a generalization of the complex physical behavior of the system. The sensible way forward to unravel this would be to generate additional translational variants of the same configurations to investigate for any physical edge dependencies or otherwise strengthen the model. We earmark this suggestion for another study. When considering some of the strain curves we also find that the prediction of the rupture point plays an important role for the max drop property. As the rupture was often predicted on a descending part of the curve any variation to the rupture point will affect the max drop property quite significantly.

We use the 20 configurations from the top candidates in the Random walk class as a test set. We sample 30 pseudo uniform strain values and use a normal load of 5 nN. The test set gave a loss 2.13 which is two orders of magnitude higher than the validation and an average absolute error for the mean friction of 0.14 and rupture accuracy of 70 %. This corresponded to an average negative R^2 score indicating that we would have been better off guessing on a constant value corresponding to the true data mean. This shows that the model is clearly not generalized. While some parts can be attributed to the overfitting of the model we believe that this is more likely to be a problem of a too small dataset. **This was just recently added so I need to incorporate this in the further discussion... It is a bit sad..**

Table 1.8: Pattern search. The values are in units nN.

Scores	Search			Data
	Tetrahedron	Honeycomb	Random walk	
$\min F_{\text{fric}}$	-0.062	-0.109	-0.061	0.0067
$\max F_{\text{fric}}$	1.089	2.917	0.660	0.0177
$\max \Delta F_{\text{fric}}$	1.062	2.081	0.629	0.5758
max drop	0.277	1.250	0.269	0.0024
Configs.				
$\min F_{\text{fric}}$	(13, 11, 14)	(14, 25, 7, 19)	No naming	(3, 9, 4)
$\max F_{\text{fric}}$	(1, 3, 1)	(2, 1, 1, 1)	No naming	(5, 3, 1)
$\max \Delta F_{\text{fric}}$	(1, 3, 1)	(2, 1, 1, 1)	No naming	(2, 1, 5, 3)
max drop	(1, 7, 1)	(3, 3, 5, 3)	No naming	(5, 3, 1)
Tetrahedron				
Honeycomb				
Random walk				

**Figure 1.15:** CAPTION

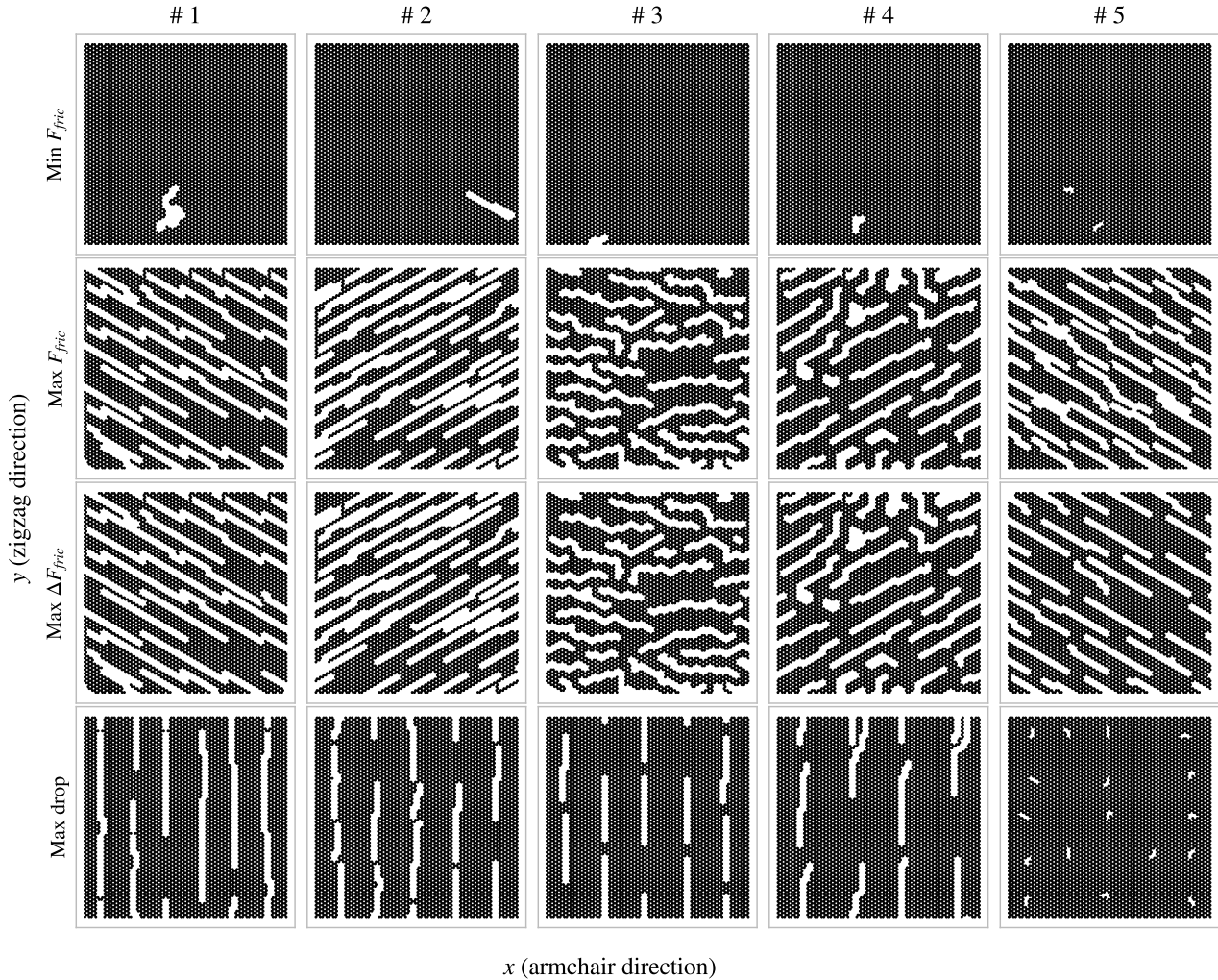


Figure 1.16: RW search top results.

1.5.2 Genetic algorithm search

For the second approach to an accelerated search, we consider the genetic algorithm. So far we have concluded that a minimization of the friction is not promising, and hence we discard this property for further studying. We have also seen that the maximum style properties often share similar top candidates, and thus we choose to only investigate the max drop property, associated with the aim of creating a negative friction coefficient. We are going to use the extended search top candidate as a basis for the genetic algorithm population algorithm search. We generate a population of 100 configurations using the settings associated with the max drop top candidate for the Tetrahedron, Honeycomb and Random walk patterns respectively. We run the search for 50 generations as we did not see much difference for any longer runs. The Tetrahedron and Honeycomb search did immediately not give any improvements as the highest scoring individual from the population was not improved through the search even though the average score was rising initially. For the Random walk, we choose to perform a genetic algorithm search for each of the top 5 candidates. Most of them gave a similar result as seen from the Tetrahedron and Honeycomb pattern with only a single new candidate generated. The score of this candidate was 0.240 nN which is a small improvement from the best score of 0.182 nN. However, from some of the other runs the population initialization provided a top score of 0.345 nN which shows that we have better hopes of optimizing this property by simply generating more configurations from the top candidate parameters. The fact that starting from an existing design did not give any useful results we attempted to start from a population of random noise as well. We made one population from mixed porosities, having even 20 individuals each for porosity $\{0.01, 0.05, 0.1, 0.2, 0.3\}$, and two populations based on a porosity of 0.25 and 0.5 respectively. This

time the algorithm improved the top candidate throughout, but the actual scores are still not impressive. The mixed porosity start gave the highest score, being 0.299 nN. When considering the corresponding patterns from the top five candidates in this search, they were all visually quite similar to the starting configurations; they still looked like random noise. Thus, we do not find signs of a generation of any noticeable patterns worth further investigating. By the use of the Grad-CAM method, we examined for any noticeable patterns for the model predictions on this mixed porosity top candidate as shown Fig. 1.17. For comparison, we included a similar examination for the top candidates in the pattern generation search with respect to the max drop category for the Tetrahedron, Honeycomb and Random walk shown Fig. 1.18 to 1.19. For the mixed porosity top candidate, the Grad-CAM method highlights some areas in the noise configuration as contributing more positively than others. However, we do not see any obvious patterns. For the more structured patterns of the Tetrahedron, Honeycomb and Random walk configurations we see in many cases throughout the straining that the cut parts are highlighted. This gives some confidence to the idea that the model does consider some of the relevant features in the pattern, but it still varies too much to make any strong conclusion. However, we notice that for certain strain values, the Grad-CAM reveals an “attention” towards the edge of the configuration. This especially relates to the top and bottom edge, which we for instance see for the Honeycomb pattern at strain 0.396 regarding the bottom edge in Fig. 1.19. Considering that the top and bottom of the configuration are not a true edge, since these are connected to the pull blocks in the simulation, this is a bit surprising. One interpretation is that the dissipation associated with the thermostat in the pull blocks might be of importance. This is not strongly supported and we simply note that as an interesting topic for further studies.

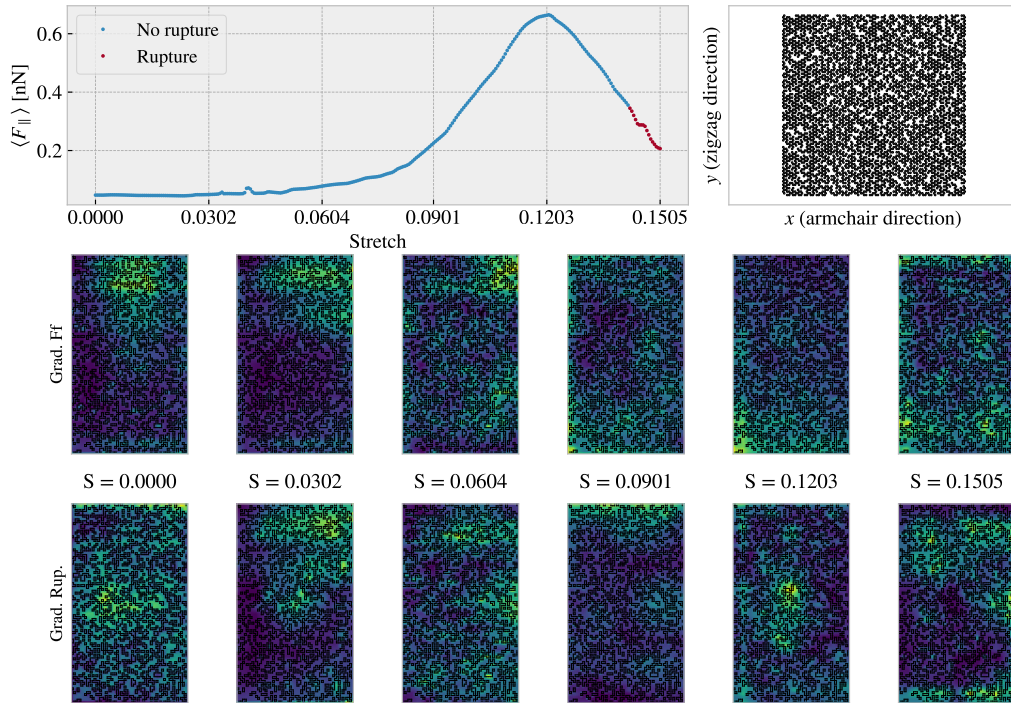


Figure 1.17: $p \in \{0.01, 0.05, 0.1, 0.2, 0.3\}$.

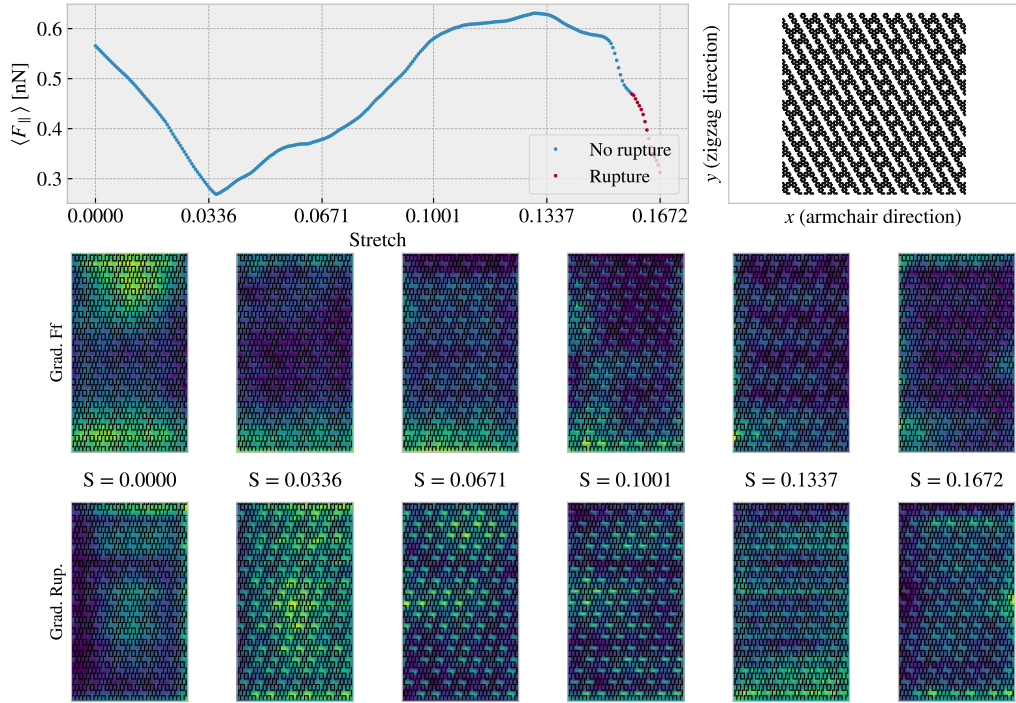


Figure 1.18: Tetrahedron (1, 7, 1), ref = (1, 4)

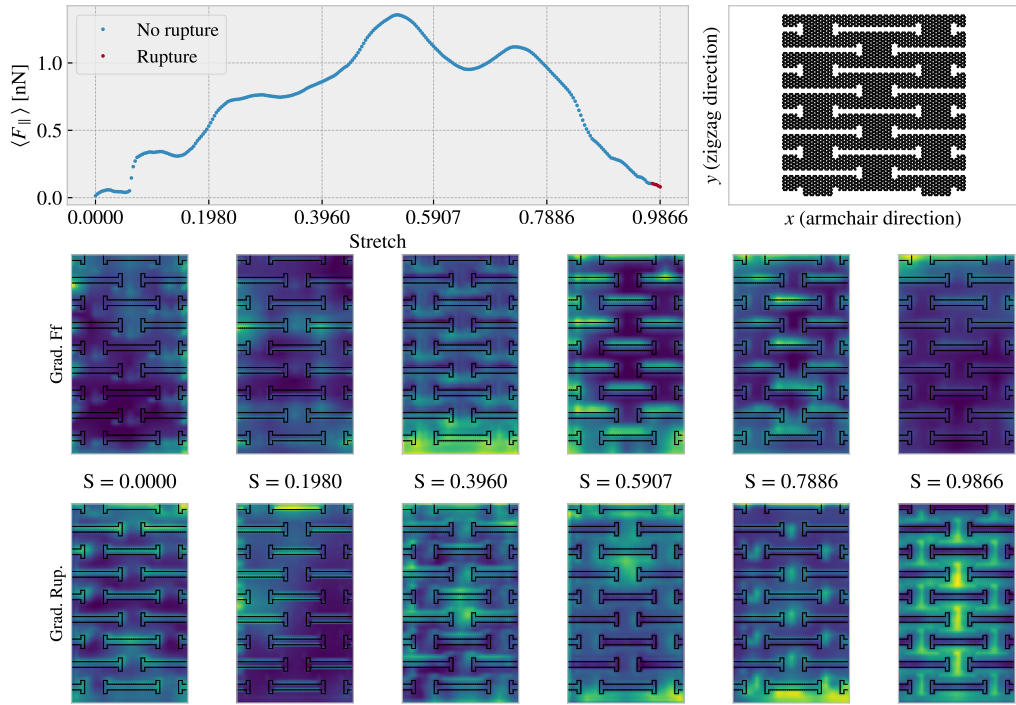
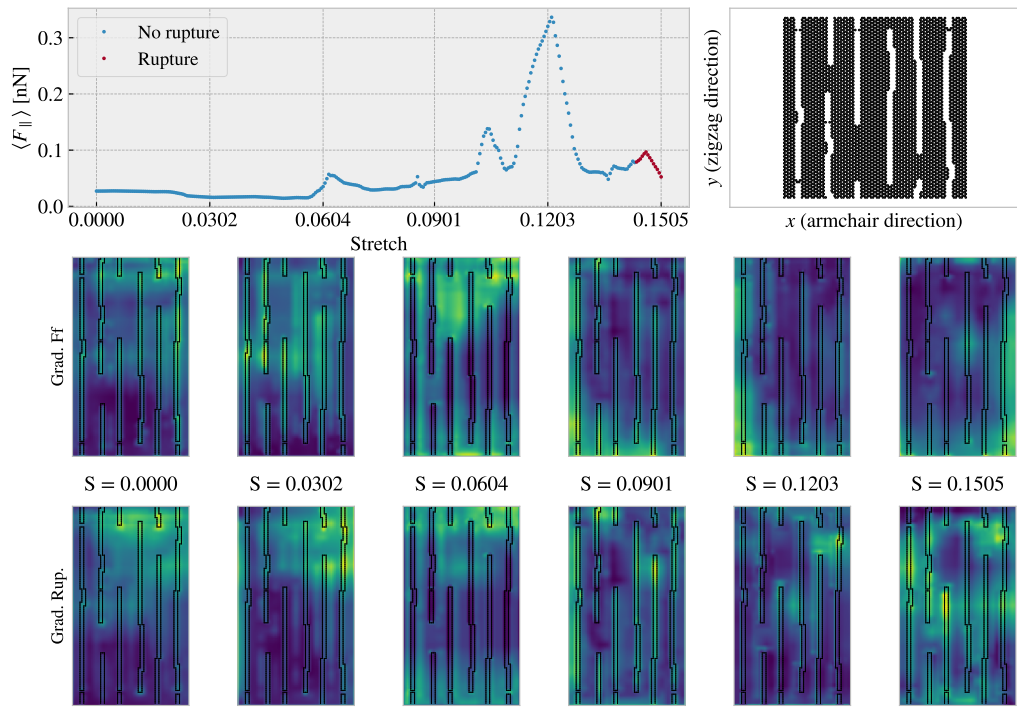


Figure 1.19: Honeycomb (3, 3, 5, 3), ref = (12, 0)

**Figure 1.20:** RW.

Appendices

Appendix A

Appendix A

Appendix A

Appendix B

Appendix B

Appendix C

Bibliography

- ¹P. Z. Hanakata, E. D. Cubuk, D. K. Campbell, and H. S. Park, “Accelerated search and design of stretchable graphene kirigami using machine learning”, *Phys. Rev. Lett.* **121**, 255304 (2018).
- ²P. Z. Hanakata, E. D. Cubuk, D. K. Campbell, and H. S. Park, “Forward and inverse design of kirigami via supervised autoencoder”, *Phys. Rev. Res.* **2**, 042006 (2020).
- ³L.-K. Wan, Y.-X. Xue, J.-W. Jiang, and H. S. Park, “Machine learning accelerated search of the strongest graphene/h-bn interface with designed fracture properties”, *Journal of Applied Physics* **133**, 024302 (2023).